Faraday Discussions

Accepted Manuscript

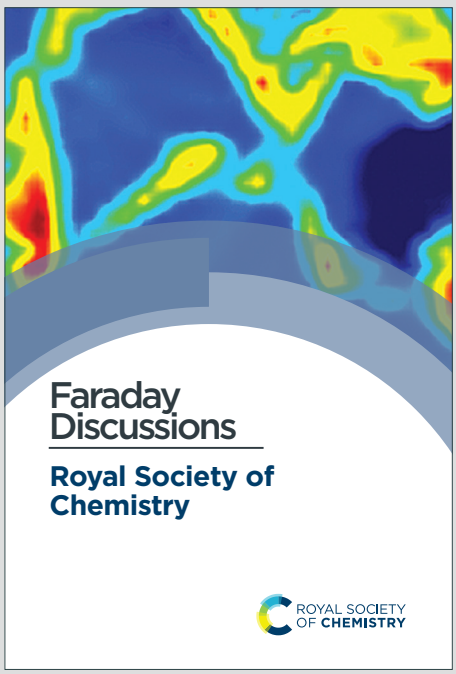

This article can be cited before page numbers have been issued, to do this please use: A. Leo, Y. arbia, A. Landi and A. Peluso, *Faraday Discuss.*, 2026, DOI: 10.1039/D6FD00012F.

ROYAL SOCIETY OF CHEMISTRY

www.rsc.org/faraday_d

View Article Online
DOI: 10.1039/D6FD00012F

First Principle calculations of the internal conversion and intersystem crossing rates of IDIC, Y6, and $PC_{70}BM$.

Anna Leo,* Yassamina Arbia, Alessandro Landi, and Andrea Peluso*

Dipartimento di Chimica e Biologia Adolfo Zambelli, Università di Salerno, Via Giovanni Paolo II, I-84084 Fisciano (SA), Italy

E-mail: anleo@unisa.it; apeluso@unisa.it

Abstract

The efficiency of OSCs is controlled by elementary processes occurring within the donor and acceptor domains and at their interface. Herein, we introduce a fully quantum mechanical, first-principles framework for quantitatively predicting the rates of these elementary electronic transitions with high accuracy and at an affordable computational cost. The approach integrates Fermi's Golden Rule with density functional theory (DFT), enabling direct evaluation of both radiative and non-radiative transition rates from the knowledge of equilibrium nuclear configurations and vibrational frequencies and normal modes. It has been shown that the method yields excellent agreement with experiments and provides new insights into the role of electronic coupling and vibronic interactions in voltage losses. Here we apply it for evaluating the internal conversion and intersystem crossing rates of IDIC, Y6, and $PC_{70}BM$.

Introduction

Organic solar cells (OSCs) are among the most attractive photovoltaic technologies owing to their potential to provide lightweight, flexible, large-area, low-cost devices,[1–6] reaching efficiencies of almost 20%.[7–9] Their operation principles are somewhat different from those of inorganic solar

View Article Online
DOI: 10.1039/D6FD00012F

cells: light absorption in organic semiconductors produces tightly bound Frenkel excitons as a consequence of the low dielectric constant of these materials.[10,11] Therefore, as in natural photosynthesis, efficient photoinduced charge dissociation relies on a donor-acceptor heterojunction, most commonly realized in the bulk-heterojunction architecture, which provides the pathway for ultrafast exciton dissociation and efficient charge separation.[12–14]

For many years, fullerene derivatives served as electron acceptors in OSCs. However, the entire class of fullerene acceptors suffers from many problems due to their weak and narrow optical absorption, limited tunability of their electronic structure, morphological and thermal instability, and high voltage losses, which ultimately limit device performances.[15,16] The introduction of non-fullerene acceptors (NFAs) has allowed many of these drawbacks to be overcome: NFAs offer strong and tunable absorption, adjustable energy levels, and improved stability, leading to significant increases in short-circuit current density and open-circuit voltage.[17–21] These recent achievements could completely turn the situation around, making OSCs able to compete with other photovoltaic technologies.[22,23]

Despite these advances, OSCs are still characterized by low open-circuit voltage (V_{oc}), which has been attributed to the presence of non-radiative charge recombination processes.[24] The maximum achievable open-circuit voltage is obtained when recombination occurs exclusively through radiative pathways.[25] In practice, OSCs operate far from this radiative limit, as demonstrated by the low electroluminescence quantum yield of OSC materials.

For OSCs to compete with other photovoltaic technologies those non radiative charge recombination paths have to be identified and suppressed. Theoretical computations can be of great help in this task, especially because in the last years robust theoretical approaches able to reliably predict the rates of non-radiative elementary processes from first principles have been developed.[26–29] Here, we discuss a theoretical approach for the reliable evaluation from first principles of the rates of elementary non-radiative processes, commonly occurring in bulk heterojunctions OSCs. This methodology has already been successfully employed to investigate

View Article Online
DOI: 10.1039/D6FD00012F

internal conversions in the azulene molecule.[30] Here, we shortly review the main steps of derivation and provide a novel rate expression, which, although completely equivalent to the previous one, is simpler to implement. The approach will be then applied to the possible decay paths of small organic molecules used as acceptors in OSCs, the real novelty of the present paper, with the attempt of providing a deeper understanding of their photophysics.

Evaluation of non-radiative decay rates.

At the first-order of the Time-Dependent Perturbation Theory (Fermi's Golden Rule), the rate of an elementary transition between the electronic states $|m>$ and $|n>$ is:

$$K_{mn} = \frac{2\pi}{\mathrm{h}} F(E,T) \tag{1}$$

with

$$F(E,T) = \sum_{\mu}\sum_{\nu} |\hat{H}'_{n\nu,m\mu}|^2 \, w_{m\mu}(T)\delta(E - E_{mn} + E_{n,\nu} - E_{m,\mu}) \tag{2}$$

where H' is the perturbation which causes the transition between the two electronic states, E_{mn} the electronic energy difference, $E_{m\mu}$ and $E_{n\nu}$ the vibrational energies, and $w_{m\mu}$ the population of the initial vibronic states:

$$w_{m\mu} = \frac{e^{-\beta E_{m\mu}}}{Tr\rho_m(\beta)}, \tag{3}$$

with $\beta = 1/kT$ and $\rho_m(\beta)$ the density operator for the vibrational motion in the initial electronic state $|m$i:

$$\rho_m(\lambda) = \sum_{nu_m} < \nu_m | e^{-\lambda E_{\nu m}} | \nu_m > \tag{4}$$

In order to avoid the infinite summations of Eq. 2, it is convenient to evaluate the Laplace transform of $F(E,T)$:[31]

View Article Online
DOI: 10.1039/D6FD00012F

$$f(\lambda) = \int_{-\infty}^{+\infty} F(\bar{E},T)e^{-\lambda\bar{E}}d\bar{E} =$$

$$1/\mathrm{Tr}\rho_m(\beta)\sum_{n\nu}\langle m\mu|\,\hat{\mathcal{H}}'\,|n\nu\rangle\, e^{-\lambda E_{n\nu}}\ \langle n\nu|\,\hat{\mathcal{H}}'\,|m\mu\rangle\, e^{-(\beta-\lambda)E_{m\mu}}\,\langle m\mu|m\mu\rangle \tag{5}$$

with $\bar{E}$ = $E - E_{mn}$. Introducing the Born-Oppenheimer approximation and integrating over the electronic coordinates:

$$f(\lambda) = Tr\hat{H}'_{mn}\rho_n(\lambda)\hat{H}''_{nm}\rho_m(\beta-\lambda)\,/\,\mathrm{Tr}\rho_m(\beta),, \tag{6}$$

which can be recast in the form:[31,32]

$$f(\lambda) = \int d\mathbf{Q} < \mathbf{Q}\,|\,\hat{H}'_{mn}\rho_n(\lambda)\hat{H}'_{nm}\rho_m(\beta-\lambda)\,|\,\mathbf{Q} > /Tr\,\rho_m(\beta) \tag{7}$$

where $\mathbf{Q}$ denotes a complete set of vibrational coordinates.

The density matrices $\rho_m(\beta - \lambda)$ and $\rho_n(\lambda)$ in the coordinate representation can be evaluated adopting the harmonic approximation for nuclear motions and making use of the well-known formula for the density matrix of the one-dimensional harmonic oscillator with frequency ω and unit mass:

$$< q\,|\,\rho(\lambda)\,|\,\bar{q} >= (2\pi\mathrm{h}\sinh(\beta\mathrm{h}\omega)/\omega)^{-1/2}$$
$$\exp[-(\omega/4\mathrm{h})\tanh(\beta\mathrm{h}\omega)(q+\bar{q})^2 - (\omega/4\mathrm{h})\coth(\beta\mathrm{h}\omega)(q-\bar{q})^2] \tag{8}$$

The density matrix for a molecular system consisting of N harmonic oscillators is obtained by simply taking the product of eq. 9 over all normal modes. The normal coordinates of one electronic state are then projected over those of the other state by using Duschinsky's transformation:

View Article Online
DOI: 10.1039/D6FD00012F

$$\mathbf{Q}_n = \mathbf{J}\mathbf{Q}_m + \mathbf{K} \tag{9}$$

where $\mathbf{J}$ is called the rotation or the Duschinsky matrix and $\mathbf{K}$ is the displacement vector.[27,33,34]

Equation 8 no longer contains computationally demanding summations over vibrational states, so that the approach allows evaluating $f(\lambda)$ in an extremely effective way, including in calculations the entire set of vibrational coordinates and the effects of the temperature, without limits on the number of vibrational states to be included. The price to pay is the mandatory use of the harmonic approximation. Harmonic approximation proved to be sufficiently accurate for reproducing spectral band shapes in several compounds.[35] Anharmonic effects are relevant for transitions occurring between two electronic states characterized by a large displacement of the nuclear equilibrium positions, as it occurs in the photoelectron spectrum of ammonia.[36,37] Use of internal rather than Cartesian coordinates can already mitigate the impact of anharmonicity, even in these difficult cases.[36,38,39] In this work, we have adopted the Cartesian coordinates, because of the small equilibrium position displacements predicted by DFT calculations.

Once $f(\lambda)$ has been evaluated, the physically meaningful quantity $F(E,T)$, which allows to evaluate the rate via Eq. 2, can be obtained by resorting to numerical inverse Laplace transformation:

$$F(\bar{E},T) = \frac{1}{2\pi i}\int f(\lambda)\exp(\lambda\bar{E})d\lambda \tag{10}$$

The above procedure has been developed for different cases: *i)* $\hat{\mathcal{H}}'_{mn}$ independent of nuclear coordinates,[40] an useful approximation for evaluating the shapes of absorption and emission bands,[35] often used in electron transfer processes too;[41] *ii)* $\hat{\mathcal{H}}'_{mn} \propto \mathbf{Q}_m$, i.e. the case of the Herzberg-Teller terms in spectroscopy ($\hat{\mathcal{H}}'_{nm} = \sum_i M_{mi}Q_{m_i}$);[42] *iii)* the case of nonadiabatic couplings,[30] in which only the terms involving the first derivative of the electronic wavefunction with respect to the vibrational coordinates are retained, while their dependence on the nuclear coordinates is neglected:

View Article Online
DOI: 10.1039/D6FD00012F

$$H'_{m\mu,n\nu} = \sum_i \left(\langle m| \frac{i\hbar\partial}{\partial Q_{mi}} |n\rangle \right)_{Q^0_{mi}} \langle m\mu| \frac{i\hbar\partial}{\partial Q_{mi}} |n\nu\rangle \tag{11}$$

Herein, we will use the case of $\hat{\mathcal{H}}'_{mn}$ independent of nuclear coordinates, for which

$$f(\lambda) = |\hat{\mathcal{H}}'_{mn}|^2 \Theta \exp[-\Delta^\dagger \mathbf{T}_n (\mathbf{T}_m + \mathbf{T}_n)^{-1} \mathbf{T}_m \Delta] \tag{12}$$

and the case of non-adiabatic couplings, for which:

$$\begin{aligned} f(\lambda) = \Theta \exp[-\Delta^\dagger \mathbf{T}_n \mathbf{A}^{-1} \mathbf{T}_m \Delta] \\ \times \left(\mathbf{S}^\dagger \frac{1}{2} \left(\mathbf{C}_n \mathbf{B}^{-1} \mathbf{C}_m - \mathbf{T}_n \mathbf{A}^{-1} \mathbf{T}_m \right)_{\mathbf{S}} \right. \\ \left. + \mathbf{S}^\dagger \left(\mathbf{T}_n \mathbf{A}^{-1} \mathbf{T}_m \Delta \Delta^\dagger \mathbf{T}_n \mathbf{A}^{-1} \mathbf{T}_m \right) \mathbf{S} \right) \end{aligned} \tag{13}$$

with

$$\Delta = -\mathbf{J}^{-1}\mathbf{K} \tag{14}$$

$$\begin{aligned} \theta = \{ \det[4\pi^2 \hbar^2 (2\sinh(\beta\hbar\boldsymbol{\Omega}_m/2))^{-2} \boldsymbol{\Omega}_m^{-1} \\ \times \sinh((\beta-\lambda)\hbar\boldsymbol{\Omega}_m) \boldsymbol{\Omega}_n^{-1} \sinh(-\lambda\hbar\boldsymbol{\Omega}_n)] \}^{-1/2} \end{aligned} \tag{15}$$

$$\mathbf{T}_m(\beta-\lambda) = \frac{\boldsymbol{\Omega}_m}{\hbar} \tanh((\beta-\lambda)\hbar\boldsymbol{\Omega}_m/2) \tag{16}$$

$$\mathbf{C}_m(\beta-\lambda) = \frac{\boldsymbol{\Omega}_m}{\hbar} \coth((\beta-\lambda)\hbar\boldsymbol{\Omega}_m/2) \tag{17}$$

$$\mathbf{T}_n(\lambda) = \mathbf{J}^\dagger \frac{\boldsymbol{\Omega}_n}{\hbar} \tanh(\lambda\hbar\boldsymbol{\Omega}_n/2)\mathbf{J} \tag{18}$$

$$\mathbf{C}_n(\lambda) = \mathbf{J}^\dagger \frac{\boldsymbol{\Omega}_n}{\hbar} \coth(\lambda\boldsymbol{\Omega}_n/2)\mathbf{J}, \tag{19}$$

$$\mathbf{A} = \mathbf{T}_m + \mathbf{T}_n \qquad \mathbf{B} = \mathbf{C}_m + \mathbf{C}_n \tag{20}$$

$$\Theta = 2^{N_{vib}} \theta \left(\frac{\det(\mathbf{T}_m + \mathbf{T}_n)}{\pi^{N_{vib}}} \right)^{-1/2} \left(\frac{\det(\mathbf{C}_m + \mathbf{C}_n)}{\pi^{N_{vib}}} \right)^{-1/2} \tag{21}$$

View Article Online
DOI: 10.1039/D6FD00012F

and

$$S_j = -i\hbar \sum_j \left(< m | \frac{\partial}{\partial Q_{mj}} | n > \right)_{Q^0_{mi}} \quad (22)$$

Expression 14 is different from that given in our previous work, because here we used a slightly different procedure to derive it, which leads to a simpler and more compact expression. Numerically, the results obtained by the two expressions are undistinguishable.

Results and Discussion

In organic solar cells nonradiative decay can occur either during exciton diffusion within the donor (D) or acceptor (A) domains or at the A/D interface, after the charge transfer (CT) state has been formed. The latter case has already been investigated in some depth, both for fullerene and non-fullerene acceptors,[43,44] so that here we will focus on the former case. We will consider only decay processes which involve the first excited singlet S_1, assuming that either sunlight does not induce excitation to higher energy states or that non-radiative transitions from those states rapidly lead to populate only S_1. As decay paths we will consider the direct internal conversion (IC) to the ground state and the intersystem crossing (ISC) to one of the triplet states that is at energy lower than S_1.

We have selected two non-fullerene acceptors, Y6 and IDIC, which proved to be among the most efficient acceptors in blend with polymer donors,[45,46] and $PC_{70}BM$, a historical fullerene derivative acceptor, which has long been used in bulk heterojunction solar cells.[44,47] The chemical structures of the selected fullerene and NFAs are shown in Figure 1. The calculated $F(\Delta E,T)$ functions for the $S_1 \rightarrow S_0$ transitions are reported in Figure 2. For Y6 and $PC_{70}BM$ the $F(\Delta E,T)$s are narrow and decay rapidly within 5000 cm^{-1}, as expected from the energy gap law. The significant contributions to

View Article Online
DOI: 10.1039/D6FD00012F

the density of states at negative wavenumbers correspond to transition involving initial excited vibrational states, populated according to Boltzmann statistics. In contrast, the $F(\Delta E,T)$ of IDIC is significantly broader, extending over more than 10 000 cm^{-1}. The resulting IC rate of IDIC is approximately three orders of magnitude larger than that of $PC_{70}BM$ and about two orders of magnitude larger than that of Y6, see Table 1, where the calculated rates are reported, together with computed and experimental energy differences (ΔE), and the magnitudes of the **K** and **S**, cf. eq.s 10 and 22, vectors.

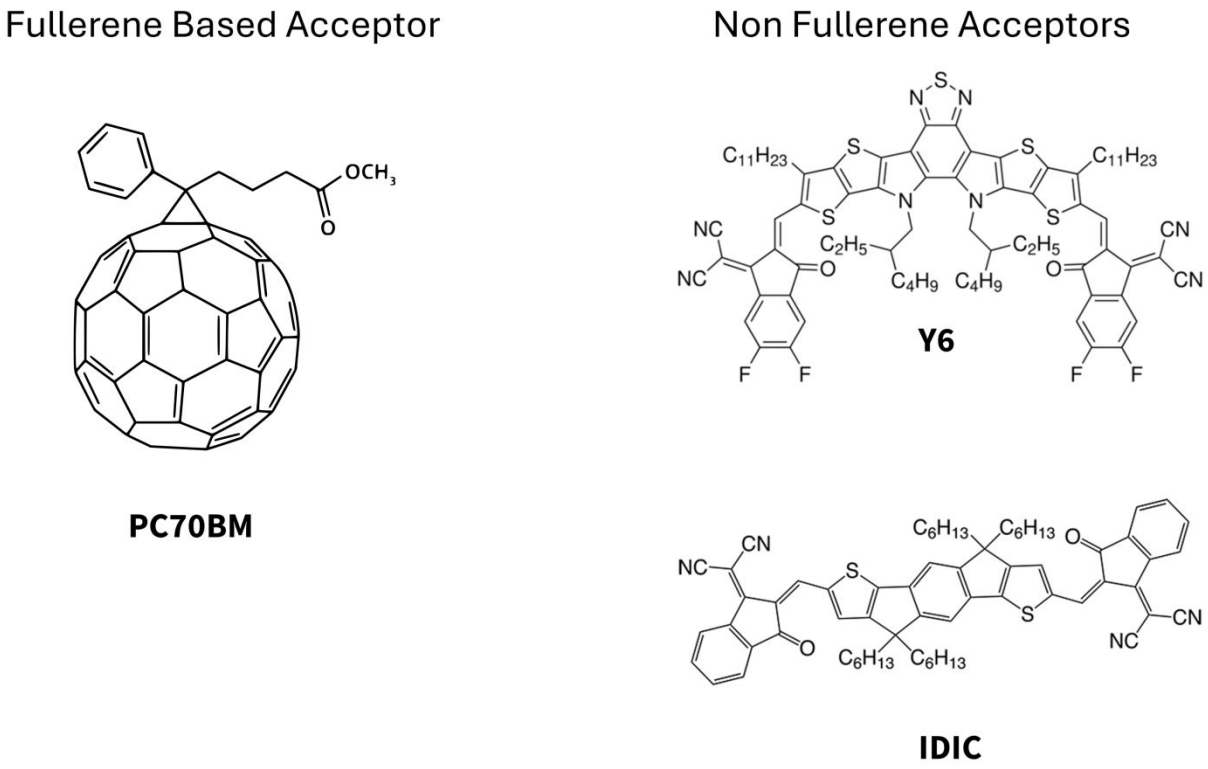

Figure 1: Chemical structures of selected fullerene acceptors and NFAs.

The pronounced rate differences can be primarily attributed to variations in the components of the **K** vectors. As shown in Table 1, the magnitude of the equilibrium position displacement vector for IDIC is substantially larger than those of Y6 and $PC_{70}BM$, which exhibit comparable values. The situation is somewhat similar to that characterizing IC in azulene, where the fast $S_1 \rightarrow S_0$ transition is mainly promoted by large displacements between the equilibrium geometries

View Article Online
DOI: 10.1039/D6FD00012F

of the two states,[30] while the slowness of the $S_2 \rightarrow S_1$ transition is attributed to a narrow $F(E,T)$, mainly due to the fact that the equilibrium geometries of the two states are similar each other.

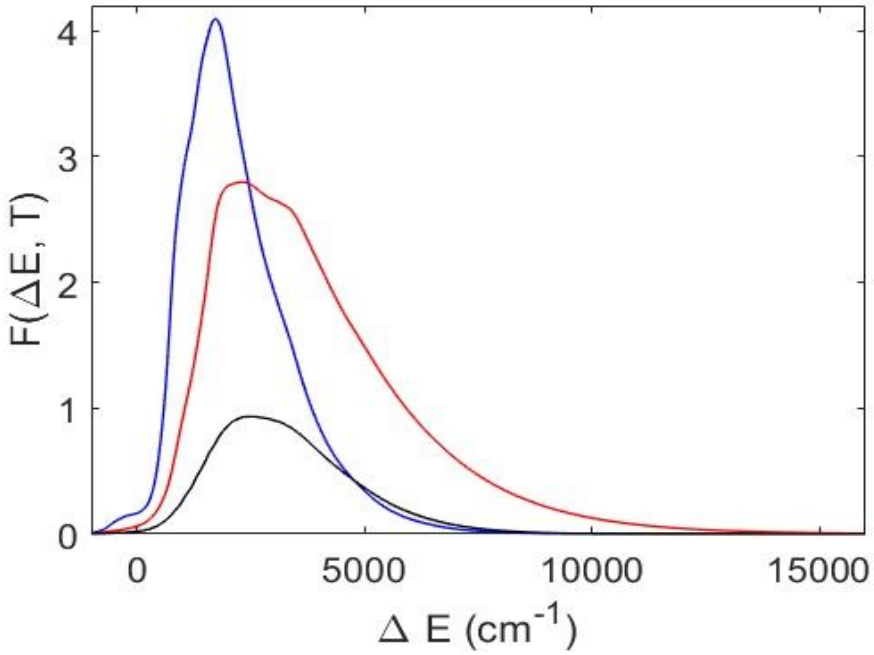

Figure 2: $F(\Delta E,T)$ at T = 298 K of the $S_1 \rightarrow S_0$ internal conversion of Y6 (blue), IDIC (red), and $PC_{70}BM$ (black) acceptors.

As concerns Y6 and $PC_{70}BM$, the difference in IC rates can instead be ascribed to differences in the nonadiabatic couplings (NACs). Indeed, the magnitude of the **S** vector (Table 1) indicates stronger nuclear kinetic coupling between the involved states in Y6 compared to $PC_{70}BM$, accounting for its comparatively faster internal conversion. For $PC_{70}BM$, both **K** and **S** are comparatively small, resulting in the slowest IC rate.

Table 1: Computed and observed energy differences (B3LYP/DFT level) between S_1 and S_0 (ΔE, eV), magnitude of the equilibrium displacement vector (**K**, Å× $amu^{1/2}$) , magnitude of non adiabatic couplings vector (**S**, $bohr^{-1}$× $amu^{-1/2}$), and calculated IC rate (k_{ic}, s^{-1}) for each selected acceptor.

Acceptor	ΔE	|**K**|	|**S**|	k_{ic}	ΔE_{exp} (eV)
$PC_{70}BM$	1.8	1.17	0.23	1.7 x 10^7	1.9
Y6	1.6	0.95	0.42	1.4 x 10^8	1.6[a]
IDIC	1.7	1.99	0.40	1.8 x 10^{10}	1.8[a]

View Article Online
DOI: 10.1039/D6FD00012F

[a] Ref.48

The calculated Jablonski diagrams for the Y6 molecule is reported in Figure 3. Here, at variance of Table 1, we have reported CAM-B3LYP results. For Y6, two triplet states lie at lower energy than S_1 after full geometry optimization of all three states. The calculated spin orbit couplings (SOC) for ISC from S_1 to the lowest energy triplet states are reported in Table 2. The calculated SOC values refer to S_1 equilibrium geometry; their coordinate dependence has been neglected here.

In order to evaluate the ISC rates we have calculated the Franck-Condon weighted densities of states (FCWDS) via Eq.s 13 and 11. The results are shown in Figure 4 for the $S_1 \rightarrow T_1$ and the $S_1 \rightarrow T_2$ transitions of Y6. Figure 4 shows that the $S_1 \rightarrow T_1$ transition does not exhibit a favourable FCWDS, because the energy difference between S_1 and T_1 is large, while the FCWDS is narrow, as it would be expected from the computed value of the reorganization energy for the $S_1 \rightarrow T_1$ transition, 64 meV, which has been reported in Table 2, together with the calculated SOC values and the resulting ISC rates. Vice versa, the ΔE for the $S_1 \rightarrow T_2$ transition fall well within the width of the corresponding FCWDS, which is slightly wider than the S_1 and T_1 one, because of the larger reorganization energy. Both the FCWDS and SOCs favours the $S_1 \rightarrow T_2$ transition, so that the latter one is predicted to be slightly faster than the $S_1 \rightarrow T_1$ one, see Table 2.

Both ISC transitions are predicted to be very slow, of the order of $10^5\ s^{-1}$, because of the

View Article Online
DOI: 10.1039/D6FD00012F

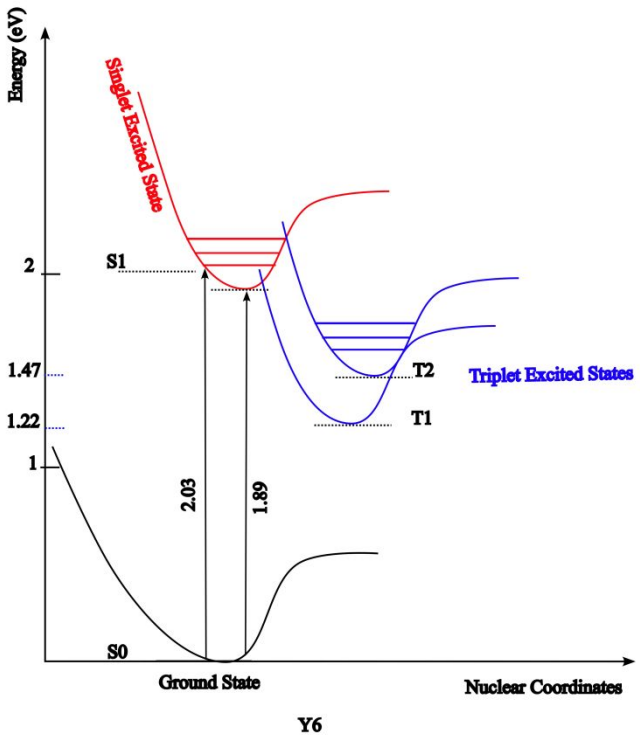

Figure 3: Calculated Jablonski diagrams of Y6; energy differences from CAM-B3LYP calculations.

Table 2: Different parameters calculated for $S_1 \rightarrow T_1$ and $S_1 \rightarrow T_2$ transitions in Y6 and IDIC.

Molecule	Transition	SOC (cm^{-1})	ΔE (eV)	FCWD (cm)	k (s^{-1})
Y6	S_1/T_1	0.058	0.81	1.14×10^{-5}	4.5×10^{4}
	S_1/T_2	0.099	0.56	2.19×10^{-5}	2.53×10^{5}
IDIC	S_1/T_1	0.102	1.0	0.0	0.0

View Article Online
DOI: 10.1039/D6FD00012F

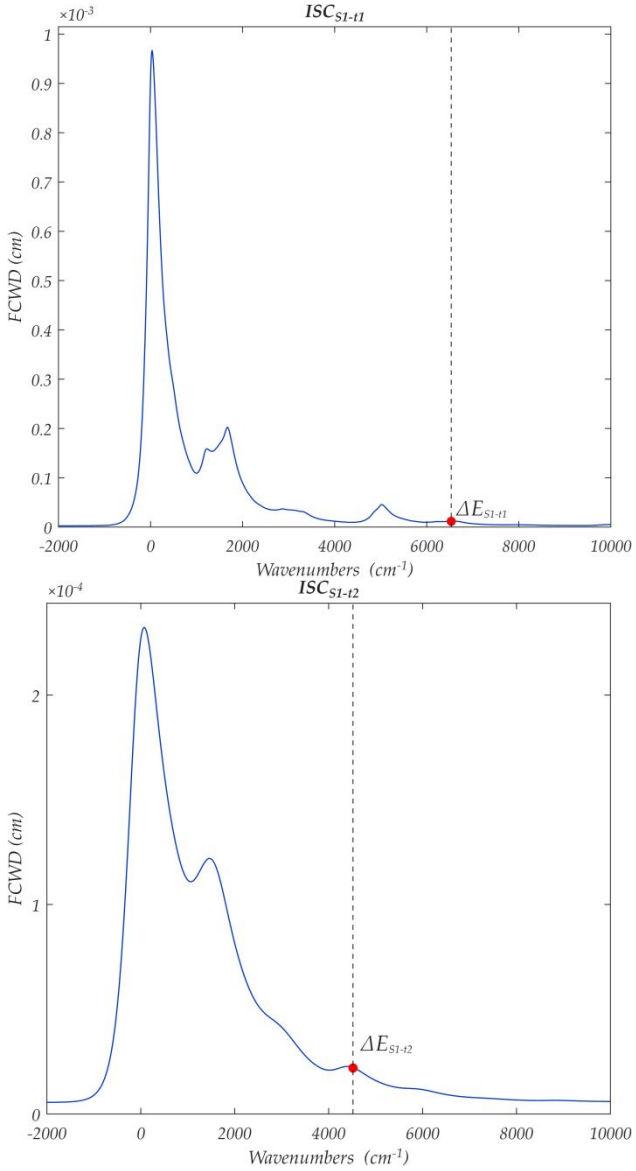

Figure 4: Franck-Condon weighted densities of states for the $S_1 \rightarrow T_1$ and the $S_1 \rightarrow T_2$ transitions of Y6 as a function of the energy difference between the initial and final state at T=298 K; the vertical line indicates the calculated (CAM-B3LYP) ΔE value.

very small values of the calculated SOCs. To the best of our knowledge experimental values for the ISC rates in Y6 have not been reported so far, but the observed high fluorescence quantum yields[49] is in line with the low ISC and IC rates predicted here. As noted above, our analysis neglect the coordinate dependence of SOCs; the latter could be included using the formulation of $f(\lambda)$ for perturbation which linearly depend on nuclear coordinates, but that task would require a very demanding computational effort. However, limited to our previous experience with the

View Article Online
DOI: 10.1039/D6FD00012F

benzophenone molecules,[50,51] for which our approach yields a quantitative prediction of the experimental rates,[52] we believe that in such rigid molecules as Y6 and also IDIC and $BC_{70}BM$ the coordinate dependence of SOC should not play a significant role.

The calculated Jablonski diagram for IDIC and the SOCs for ISC from S_1 to T_1, calculated at the S_1 equilibrium geometry, are reported in Figure 5 and Table 2, respectively. Two triplet states are found to lie at lower energy than S_1 after full geometry optimizations of the lowest two singlet and three triplet states. For one of them, T_2, the calculated SOC is vanishingly small, so that only the $S_1 \rightarrow T_1$ transition is predicted to be possible.

The FCWDS for the $S_1 \rightarrow T_1$ transition is shown in Figure 6 as a function of the energy difference between the initial and final state; the vertical line indicates the calculated (CAMB3LYP) ΔE. Even in this case the ΔE of the transition falls well outside the energy range in which the FCWDS is significantly different from zero, which, considering also that the calculated SOC is very small, makes the transition rates to be vanishingly small.

To the best of our knowledge, even for IDIC experimental values for the ISC rates have not been reported in the literature. The fluorescence quantum yield has been reported to be ca. 1%;[53] such a low value can be well explained by the comparatively high IC rate of Table 2, without the necessity of invoking fast ISC decay processes.

As concerns ISC in $PC_{70}BM$, the situation is much more complicated because at the S_1 equilibrium geometries seven triplet states are predicted to lie below S_1, without performing any geometry optimizations of the triplet states. The calculations of the ISC rates

View Article Online
DOI: 10.1039/D6FD00012F

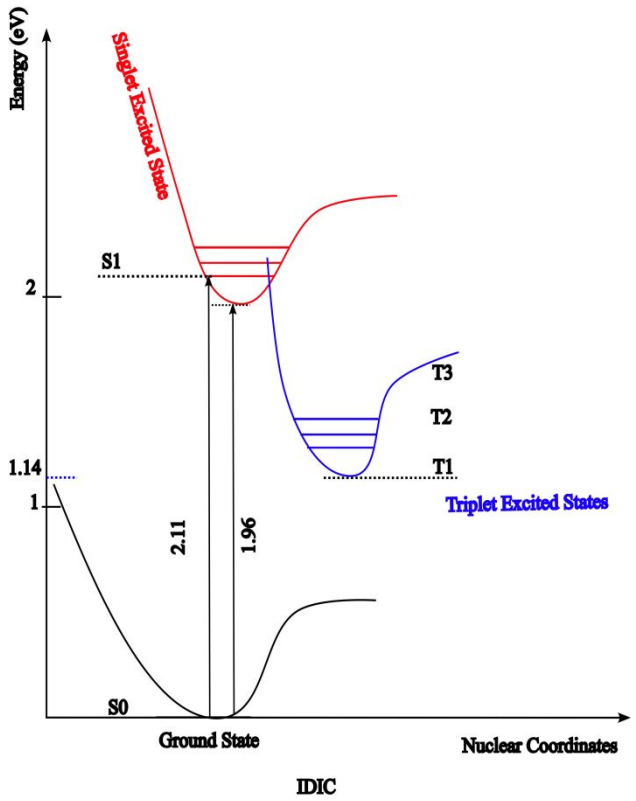

Figure 5: Calculated Jablonski diagrams of IDIC; energy differences from CAM-B3LYP calculations.

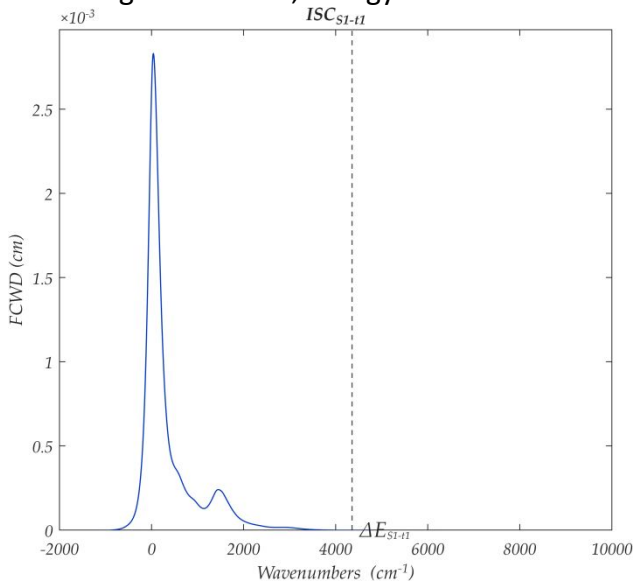

Figure 6: Franck-Condon weighted density of states for the $S_1 \rightarrow T_1$ transition of IDIC as a function of the energy difference between the initial and final state; T=298 K. The vertical line indicates the calculated (CAM-B3LYP) ΔE value.

View Article Online
DOI: 10.1039/D6FD00012F

would therefore require a tremendous computational effort, which is far beyond our actual capabilities.

Conclusions

In conclusion, we have presented a theoretical approach based on Time-Dependent Perturbation Theory and the use of the density matrix for vibrational motion for treating, in the limits of the harmonic approximation,[4,30] quantum dynamics of IC and ISC processes. These processes commonly occur in organic solar cells, so that the approach represents a potentially powerful tool for investigating in silico the efficiency of novel organic molecules to be used in devices, enabling a quantitative evaluation of how vibronic interactions control the efficiency of decay paths, and allowing for going beyond qualitative interpretations of excited-state dynamics. The approach has then been applied to the calculation of IC and ISC rates of a set of fullerene and non fullerene acceptors, IDIC, Y6, and PC70BM, in the attempt of better understanding their photophysics. For IDIC and Y6 the results are in line with experimental observations,[49,53] which assign to Y6 a much larger fluorescence quantum yields than IDIC.

Computational Details

The equilibrium geometries, normal modes, and vibrational frequencies of both fullerene and NFAs were obtained at the DFT level using the B3LYP functional, including Grimme's D3 dispersion,[54] with the 6-31+G(d,p) basis set, which has been proved to yield sufficiently accurate results, and energies in line with experimental values.[30,44,46,55–57] The Gaussian package have been used for electronic wavefunction computations.[58] Time-dependent DFT (TDDFT) has been used for all the excited states. All (3N-6) real frequencies have been obtained in all cases. In the molecules under study, all alkyl substituents have been replaced by methyl groups, as usual.[59–62].

View Article Online
DOI: 10.1039/D6FD00012F

The solvent contribution in both ground and excited states has been included by using the Polarizable Continuum Model (PCM)[63] as implemented in the same software. Non adiabatic coupling elements have been computed at S_1 geometry for all the systems at DFT level with the same functional and basis-set using the Q-Chem software.[64] The SOC matrix elements have been computed at the TD-DFT level at the S1 state geometry, using the RI-JK approximation as implemented in ORCA 6.0[65]

$F(\Delta E,T)$s have been computed by using a development version of the MolFC package, available on request from the authors.[26] $f(\lambda)$s were sampled over a wide interval of 8 x 10^5 cm^{-1} using 2^{10} time steps and a four-term Blackman-Harris window function, necessary to avoid boundary and spectral leakage problems. The inverse transforms have been carried out using the inverse Fast Fourier transform (FFT) algorithm implemented in MATLAB.

References

(1) Li, G.; Zhu, R.; Yang, Y. Polymer solar cells. *Nature Photonics* 2012, *6*, 153–161.

(2) He, Z.; Wu, H.; Cao, Y. Recent advances in polymer solar cells: realization of high device performance by incorporating water/alcohol-soluble conjugated polymers as electrode buffer layer. *Adv. Mater.* 2014, *26*, 1006–1024.

(3) Heeger, A. J. 25th anniversary article: bulk heterojunction solar cells: understanding the mechanism of operation. *Adv. Mater.* 2014, *26*, 10–28.

(4) Landi, A.; Ricci, G.; Olivier, Y.; Capobianco, A.; Peluso, A. Toward Efficient Modeling of Nonradiative Decay in Extended INVEST: Overcoming Computational Challenges in Quantum Dynamics Simulations. *J. Phys. Chem. Lett.* 2024, *15*, 11042–11050.

(5) Huang, Y.; Kramer, E. J.; Heeger, A. J.; Bazan, G. C. Bulk heterojunction solar cells: morphology and performance relationships. *Chem. Rev.* 2014, *114*, 7006–7043.

View Article Online
DOI: 10.1039/D6FD00012F

(6) Lu, L.; Zheng, T.; Wu, Q.; Schneider, A. M.; Zhao, D.; Yu, L. Recent advances in bulk heterojunction polymer solar cells. *Chemical reviews* 2015, *115*, 12666–12731.

(7) Sun, R.; Wu, Y.; Yang, X.; Gao, Y.; Chen, Z.; Li, K.; Qiao, J.; Wang, T.; Guo, J.; Liu, C.; Hao, X.; Zhu, H.; Min, J. Single-Junction Organic Solar Cells with 19.17% Efficiency Enabled by Introducing One Asymmetric Guest Acceptor. *Adv. Mater.* 2022, *34*, 2110147.

(8) Sun, J.; Ma, X.; Zhang, Z.; Yu, J.; Zhou, J.; Yin, X.; Yang, L.; Geng, R.; Zhu, R.; Zhang, F.; Tang, W. Dithieno[3,2-b:2’,3’-d]pyrrol Fused Nonfullerene Acceptors Enabling Over 13% Efficiency for Organic Solar Cells. *Adv. Mater.* 2018, *30*, 1707150.

(9) Fu, J.; Fong, P. W. K.; Liu, H.; Huang, C.-S.; Lu, X.; Lu, S.; Abdelsamie, M.; Kodalle, T.; Sutter-Fella, C. M.; Yang, Y.; Li, G. 19.31% binary organic solar cell and low non-radiative recombination enabled by non-monotonic intermediate state transition. *Nat. Commun.* 2023, *14*, 1760.

(10) Kounavis, P.; Symeonidis, I. Exciton dissociation mechanism and exciton density in organic semiconductors by modulated-photocurrent spectroscopy. *Physical Review Materials* 2024, *8*, 113807.

(11) Valencia, A. M.; Bischof, D.; Anhäuser, S.; Zeplichal, M.; Terfort, A.; Witte, G.; Cocchi, C. Excitons in organic materials: revisiting old concepts with new insights. *Electronic Structure* 2023, *5*, 033003.

(12) Ie, Y.; Yamada, H. Recent research trends toward high-efficiency OPVs. *Journal of Photochemistry and Photobiology C: Photochemistry Reviews* 2025, *63*, 100690.

(13) Ambrosio, F.; Wiktor, J.; Landi, A.; Peluso, A. Charge Localization in Acene Crystals from Ab Initio Electronic Structure. *J. Phys. Chem. Lett.* 2023, *14*, 3343–3351.

(14) Kisslinger, R.; Hua, W.; Shankar, K. Bulk heterojunction solar cells based on blends of conjugated polymers with II–VI and IV–VI inorganic semiconductor quantum dots.

View Article Online
DOI: 10.1039/D6FD00012F

Polymers 2017, *9*, 35.

(15) Yuan, J.; Huang, T.; Cheng, P.; Zou, Y.; Zhang, H.; Yang, J. L.; Chang, S.-Y.; Zhang, Z.; Huang, W.; Wang, R., et al. Enabling low voltage losses and high photocurrent in fullerene-free organic photovoltaics. *Nature communications* 2019, *10*, 570.

(16) Yang, J.; Li, Q.-S.; Li, Z.-S. Theoretical design of asymmetric A–D 1 A' D 2–A type non-fullerene acceptors for organic solar cells. *Phys. Chem. Chem. Phys.* 2021, *23*, 12321–12328.

(17) Liu, W.; Xu, X.; Yuan, J.; Leclerc, M.; Zou, Y.; Li, Y. Low-bandgap non-fullerene acceptors enabling high-performance organic solar cells. *ACS Energy Letters* 2021, *6*, 598–608.

(18) Yan, C.; Barlow, S.; Wang, Z.; Yan, H.; Jen, A. K.-Y.; Marder, S. R.; Zhan, X. Nonfullerene acceptors for organic solar cells. *Nature Reviews Materials* 2018, *3*, 1–19.

(19) Cheng, P.; Li, G.; Zhan, X.; Yang, Y. Next-generation organic photovoltaics based on non-fullerene acceptors. *Nature Photonics* 2018, *12*, 131–142.

(20) Zhu, L.; Zhang, M.; Zhong, W.; Leng, S.; Zhou, G.; Zou, Y.; Su, X.; Ding, H.; Gu, P.; Liu, F., et al. Progress and prospects of the morphology of non-fullerene acceptor based high-efficiency organic solar cells. *Energy & Environmental Science* 2021, *14*, 4341–4357.

(21) Zhang, G.; Zhao, J.; Chow, P. C.; Jiang, K.; Zhang, J.; Zhu, Z.; Zhang, J.; Huang, F.; Yan, H. Nonfullerene acceptor molecules for bulk heterojunction organic solar cells. *Chemical reviews* 2018, *118*, 3447–3507.

(22) Zhao, F.; Zhang, H.; Zhang, R.; Yuan, J.; He, D.; Zou, Y.; Gao, F. Emerging approaches in enhancing the efficiency and stability in non-fullerene organic solar cells. *Advanced Energy Materials* 2020, *10*, 2002746.

(23) Luo, D.; Jang, W.; Babu, D. D.; Kim, M. S.; Wang, D. H.; Kyaw, A. K. K. Recent progress in organic solar cells based on non-fullerene acceptors: materials to devices.

View Article Online
DOI: 10.1039/D6FD00012F

Journal of Materials Chemistry A 2022, *10*, 3255–3295.

(24) Benduhn, J.; Tvingstedt, K.; Piersimoni, F.; Ullbrich, S.; Fan, Y.; Tropiano, M.; McGarry, K. A.; Zeika, O.; Riede, M. K.; Douglas, C. J.; Barlow, S.; Marder, S. R.; Neher, D.; Spoltore, D.; Vandewal, K. Intrinsic non-radiative voltage losses in fullerenebased organic solar cells. *Nat. Energy* 2017, *2*, 17053.

(25) Azzouzi, M.; Yan, J.; Kirchartz, T.; Liu, K.; Wang, J.; Wu, H.; Nelson, J. Nonradiative Energy Losses in Bulk-Heterojunction Organic Photovoltaics. *Phys. Rev. X* 2018, *8*, 031055.

(26) Borrelli, R.; Peluso, A. Dynamics of Radiationless Transitions in Large Molecular Systems: A Franck-Condon Based Method Accounting for Displacements and Rotations of All the Normal Coordinates. *J. Chem. Phys.* 2003, *119*, 8437–8448.

(27) Borrelli, R.; Peluso, A. Elementary Electron Transfer Reactions: From Basic Concepts to Recent Computational Advances. *WIREs: Comput. Mol. Sci.* 2013, *3*, 542–559.

(28) Landi, A. Charge Mobility Prediction in Organic Semiconductors: Comparison of Second-Order Cumulant Approximation and Transient Localization Theory. *J. Phys. Chem. C* 2019, *123*, 18804–18812.

(29) Niu, Y.; Li, W.; Peng, Q.; Geng, H.; Yi, Y.; Wang, L.; Nan, G.; Wang, D.; Shuai, Z. MOlecular MAterials Property Prediction Package (MOMAP) 1.0: a software package for predicting the luminescent properties and mobility of organic functional materials. *Mol. Phys.* 2018, *116*, 1078–1090.

(30) Landi, A.; Landi, A.; Leo, A.; Peluso, A. The rates of non-adiabatic processes in large molecular systems: Toward an effective full-dimensional quantum mechanical approach. *J. Chem. Phys.* 2024, *160*, 174114.

View Article Online
DOI: 10.1039/D6FD00012F

(31) Kubo, R.; Toyozawa, Y. Application of the Method of Generating Function to Radiative and Non-Radiative Transitions of a Trapped Electron in a Crystal. *Prog. Theor. Phys.* 1955, *13*, 160–182.

(32) Borrelli, R.; Peluso, A. The Temperature Dependence of Radiationless Transition Rates from Ab Initio Computations. *Phys. Chem. Chem. Phys.* 2011, *13*, 4420–4426.

(33) Duschinsky, F. *Acta Physicochim. USSR* 1937, *7*, 551–566.

(34) Sharp, T. E.; Rosenstock, H. M. Franck—Condon Factors for Polyatomic Molecules. *J. Chem. Phys.* 1964, *41*, 3453–3463.

(35) Capobianco, A.; Borrelli, R.; Landi, A.; Velardo, A.; Peluso, A. Absorption Band Shapes of a Push-Pull Dye Approaching the Cyanine Limit: A Challenging Case for First Principle Calculations. *J. Phys. Chem. A* 2016, *120*, 5581–5589.

(36) Peluso, A.; Borrelli, R.; Capobianco, A. Photoelectron Spectrum of Ammonia, a Test Case for the Calculation of Franck–Condon Factors in Molecules Undergoing Large Geometrical Displacements upon Photoionization. *J. Phys. Chem. A* 2009, *113*, 14831–14837.

(37) Capobianco, A.; Borrelli, R.; Noce, C.; Peluso, A. Franck-Condon Factors in Curvilinear Coordinates: The Photoelectron Spectrum of Ammonia. *Theor. Chem. Acc.* 2012, *131*, 1181.

(38) Borrelli, R.; Peluso, A. The Vibrational Progressions of the $\tilde{N} \leftarrow \tilde{V}$ Electronic Transition of Ethylene. A Test Case for the Computation of Franck-Condon Factors of Highly Flexible Photoexcited Molecules. *J. Chem. Phys.* 2006, *125*, 194308–8.

(39) Landi, A.; Padula, D. Optimising Conformational Effects on Thermally Activated Delayed Fluorescence. *J. Mater. Chem. C* 2022, *10*, 10699–10707.

(40) Borrelli, R.; Peluso, A. The Temperature Dependence of Radiationless Transition Rates from Ab Initio Computations. *Phys. Chem. Chem. Phys.* 2011, *13*, 4420–4426.

View Article Online
DOI: 10.1039/D6FD00012F

(41) Leo, A.; Ambrosio, F.; Landi, A.; Peluso, A. Electron Transfer Rates in Solution: Toward a Predictive First Principle Approach. *Chemistry* 2023, *5*, 97–105.

(42) Borrelli, R.; Thoss, M.; Wang, H.; Domcke, W. Quantum Dynamics of Electron-Transfer Reactions: Photoinduced Intermolecular Electron Transfer in a Porphyrin-Quinone Complex. *Mol. Phys.* 2012, *110*, 751–763.

(43) Landi, A.; Landi, A.; Velardo, A.; Peluso, A. Efficient Charge Dissociation of Triplet Excitons in Bulk Heterojunction Solar Cells. *ACS Appl. Energy Mater.* 2022, *5*, 10815– 10824.

(44) Landi, A.; Padula, D.; Peluso, A. Fast Nonradiative Decay Paths in Organic Solar Cells: Implications for Designing More Efficient Photovoltaic Systems. *ACS Appl. Energy Mater.* 2024, *7*, 707–714.

(45) Zhang, G.; Zhao, J.; Chow, P. C. Y.; Jiang, K.; Zhang, J.; Zhu, Z.; Zhang, J.; Huang, F.; Yan, H. Nonfullerene Acceptor Molecules for Bulk Heterojunction Organic Solar Cells. *Chem. Rev.* 2018, *118*, 3447–3507.

(46) Zhou, R.; Jiang, Z.; Yang, C.; Yu, J.; Feng, J.; Adil, M. A.; Deng, D.; Zou, W.; Zhang, J.; Lu, K.; Ma, W.; Gao, F.; Wei, Z. All-small-molecule organic solar cells with over 14% efficiency by optimizing hierarchical morphologies. *Nat. Commun.* 2019, *10*, 5393.

(47) Kyaw, A. K. K.; Wang, D. H.; Wynands, D.; Zhang, J.; Nguyen, T.-Q.; Bazan, G. C.; Heeger, A. J. Improved Light Harvesting and Improved Efficiency by Insertion of an Optical Spacer (ZnO) in Solution-Processed Small-Molecule Solar Cells. *Nano Lett.* 2013, *13*, 3796–3801.

(48) Zhou, R.; Jiang, Z.; Yang, C.; Yu, J.; Feng, J.; Adil, M. A.; Deng, D.; Zou, W.; Zhang, J.; Lu, K., et al. All-small-molecule organic solar cells with over 14% efficiency by optimizing hierarchical morphologies. *Nature communications* 2019, *10*, 5393.

View Article Online
DOI: 10.1039/D6FD00012F

(49) Zou, X.; Wen, G.; Hu, R.; Dong, G.; Zhang, C.; Zhang, W.; Huang, H.; Dang, W. An Insight into the Excitation States of Small Molecular Semiconductor Y6. *Molecules* 2020, *25*.

(50) Velardo, A.; Borrelli, R.; Capobianco, A.; Landi, A.; Peluso, A. Disentangling Electronic and Vibrational Effects in the Prediction of Band Shapes for Singlet-Triplet Transitions. *J. Phys. Chem. C* 2019, *123*, 14173–14179.

(51) Velardo, A.; Landi, A.; Borrelli, R.; Peluso, A. Reliable Predictions of Benzophenone Singlet–Triplet Transition Rates: A Second-Order Cumulant Approach. *J. Phys. Chem.* A 2021, *125*, 43–49.

(52) Aloise, S.; Ruckebusch, C.; Blanchet, L.; Réhault, J.; Buntinx, G.; Huvenne, J.-P. The Benzophenone S1(n,π*) → T1(n,π*) States Intersystem Crossing Reinvestigated by Ultrafast Absorption Spectroscopy and Multivariate Curve Resolution. *J. Phys. Chem. A* 2008, *112*, 224–231.

(53) Li, S.; Zhao, Y.; Yu, J.; Wang, G.; Liu, T.; Ding, L.; Fang, Y. Quadrupolar IDIC chromophores exhibiting strong two-photon absorption beyond 1000 nm. *SSRN* 2026, 1–18.

(54) Grimme, S.; Antony, J.; Ehrlich, S.; Krieg, H. A Consistent and Accurate ab initio Parametrization of Density Functional Dispersion Correction (DFT-D) for the 94 Elements H-Pu. *J. Chem. Phys.* 2010, *132*, 154104.

(55) Collins, S. D.; Proctor, C. M.; Ran, N. A.; Nguyen, T.-Q. Understanding Open-Circuit Voltage Loss through the Density of States in Organic Bulk Heterojunction Solar Cells. *Adv. Energy Mater.* 2016, *6*, 1501721.

(56) Clarke, T.; Ballantyne, A.; Jamieson, F.; Brabec, C.; Nelson, J.; Durrant, J. Transient Absorption Spectroscopy of Charge Photogeneration Yields and Lifetimes in a Low Bandgap Polymer/Fullerene Film. *Chem. Commun.* 2008, *1*, 89–91.

View Article Online
DOI: 10.1039/D6FD00012F

(57) Djurovich, P. I.; Mayo, E. I.; Forrest, S. R.; Thompson, M. E. Measurement of the lowest unoccupied molecular orbital energies of molecular organic semiconductors. *Organic Electronics* 2009, *10*, 515–520.

(58) M. J. Frisch. et al., Gaussian 16 Revision C.01. 2016; Gaussian Inc. Wallingford CT.

(59) Zhang, G. et al. Delocalization of Exciton and Electron Wavefunction in non-Fullerene Acceptor Molecules Enables Efficient Organic Solar Cells. *Nat. Commun.* 2020, *11*, 3943.

(60) Gertsen, A. S.; Sørensen, M. K.; Andreasen, J. W. Nanostructure of organic semiconductor thin films: Molecular dynamics modeling with solvent evaporation. *Phys. Rev. Mater.* 2020, *4*, 075405.

(61) Landi, A.; Padula, D. Multiple Charge Separation Pathways in New-Generation Non-Fullerene Acceptors: a Computational Study. *J. Mater. Chem. A* 2021, *9*, 24849–24856.

(62) Padula, D.; Barneschi, L.; Peluso, A.; Cinaglia, T.; Landi, A. Towards a fast machine-learning-assisted prediction of the mechanoelectric response in organic crystals. *J. Mater. Chem. C* 2023, *11*, 12297–12306.

(63) Miertuš, S.; Scrocco, E.; Tomasi, J. Electrostatic Interaction of a Solute with a Continuum. A Direct Utilization of Ab Initio Molecular Potentials for the Prevision of Solvent Effects. *Chem. Phys.* 1981, *55*, 117–129.

(64) Shao, Y. et al. Advances in molecular quantum chemistry contained in the Q-Chem 4 program package. *Mol. Phys.* 2014, *113*, 184–215.

(65) Neese, F. The ORCA program system. *WIREs Comput. Mol. Sci.* 2011, *2*, 73–78.

All data supporting the findings of this study are included within the article, its figures and tables.

View Article Online
DOI: 10.1039/D6FD00012F